



Title	Air bubbles and air-hydrate crystals in the Vostok ice core
Author(s)	Lipenkov, Vladimir Ya.
Citation	Physics of Ice Core Records, 327-358
Issue Date	2000
Doc URL	http://hdl.handle.net/2115/32474
Type	proceedings
Note	International Symposium on Physics of Ice Core Records. Shikotsukohan, Hokkaido, Japan, September 14-17, 1998.
File Information	Lipenkov_final.pdf



[Instructions for use](#)

Air bubbles and air-hydrate crystals in the Vostok ice core

Vladimir Ya. Lipenkov

Arctic and Antarctic Research Institute, St. Petersburg 199397, RUSSIA

(Present address: Institute of Low Temperature Science, Hokkaido University, N19W8, Sapporo 060-0819, JAPAN)

Abstract: The geometrical properties of air-bubble and air-hydrate ensembles in the 3310-m deep Vostok core and in other ice cores were studied. The principle results are the following: 1) the size and abundance of air bubbles in polar ice depend on the temperature and accumulation rate prevailing over the time of the snow-ice transformation, 2) the climate signal imposed on the bubble properties at pore close-off is only slightly modified in the course of the bubble-hydrate transition (500–1250 m at present time at Vostok) and in the first, transient, phase of air-hydrate crystal growth (1150–1500 m); as a consequence, the last four glacial-interglacial cycles are resolved in variations of the number and size of air inclusions along the Vostok ice core, and 3) the air-bubble and air-hydrate records from polar ice cores can provide an independent experimental constraint on the temperature-accumulation relations in the past.

1. Introduction

As a result of snow densification and pore closure processes in the melt-free regions of polar ice sheets, significant amount of firn air (~10% of firn volume) becomes trapped in ice as air bubbles. Investigations of the first deep Antarctic ice core recovered at Byrd Station [1] revealed that air bubbles disappear in ice below 1200 m. This was interpreted by Miller [2] as a transformation of air occluded in ice matrix to mixed air clathrate hydrate at pressures exceeding the dissociation pressure at the in situ temperature. Thirteen years later, the air-hydrate crystals were observed for the first time in the fresh ice core from Dye-3,

Greenland by Shoji and Langway [3]. X-ray diffraction work by Hondoh and others [4] identified the crystallographic structure of clathrates from Dye-3 core as the Stackelberg structure II.

Studies of air inclusions (i.e., bubbles and air-hydrate crystals) in polar ice cores are particularly important for two reasons. First, the air occluded in ice is considered to be our primary natural archive of past changes in atmospheric composition including those of greenhouse gases [5–7] and of the isotopic composition of the major air constituents [8, 9]. The processes associated with air clathration in the transition zone and air-hydrate decomposition (after coring) in the ice cores

could affect the interpretation of gas analyses [7, 9–11]. A great deal of additional interest in this topic was generated by the recent discovery of extreme fractionation of gases in bubbles and clathrate hydrates within the transition zone at Vostok [12]. The latter finding, along with reports of hydrate crystal growth observed in the Vostok [13, 14] and GRIP [15] cores clearly support a significant diffusivity in ice of N_2 and O_2 molecules [16] that were until recently assumed to have negligible diffusion and dissolution in the ice lattice.

Second, independently of gas composition, the geometrical properties of air inclusions in ice are thought to store information about past climate changes. Earlier studies [17, 18] revealed climate-related variations of air-bubble sizes and concentrations at different depths in the Vostok core. The sizes (number concentrations) of bubbles were found to be smaller (greater) in ice formed under glacial conditions than in Holocene ice. Similar variations were later reported for the air-hydrate crystals in the Vostok [13], GRIP [15] and Dome F [19] cores. Finally, the extension of the Vostok core down to 3310-m depth (age of ice ~ 410 kyr [20]) has allowed four glacial-interglacial cycles to be clearly distinguished in the composite record of air-bubble and air-hydrate geometrical characteristics [21, 22]. These results suggest that, despite the thick transition zone (500 to 1250 m at Vostok) and complexity involved in air clathration, the climate signal transfers from air bubbles to air hydrates.

Recent developments in the phenomenology of air-hydrate occurrence in polar ice [23, 24, 39], as well as advance in model simulation of the bubble-clathrate

transformation [25, 26] indicate a consistent theory of air-hydrate formation and evolution in polar ice sheets.

It is the purpose of this paper to contribute to these studies by a thorough reanalysis of relevant data obtained at Vostok in the 1980s and 1990s [17, 18, 21, 22, 27–32]. The focus is on the evolution of geometrical properties of the air-bubble and air-hydrate ensembles throughout the upper 3310 m of ice core, that is, down to the limit of undisturbed climatic record at Vostok [33]. There is particular emphasis on the origin of the climate signal in air bubbles and its possible alteration during bubble-hydrate transition.

2. Experimental procedures

The ice cores used in this study were retrieved from the deep boreholes 3G, 4G, and 5G drilled at Vostok Station by the drilling group from the St. Petersburg Mining Institute. The experimental data set discussed here includes precise ice density [30] and air content [28, 29] profiles, the results of direct measurements of pressure within individual air bubbles [30], and the data from thick-section analyses [17, 18, 21, 31]. Except for air content, all measurements were performed on unrelaxed ice, that is either on the fresh ice core soon after drilling, or on ice samples stored at a temperature of -55 ± 2 °C, which is low enough to prevent (at least during the first 5 years after ice recovery) significant decompression of air bubbles and decomposition of air hydrates [27, 34].

2.1. Thick-section analysis

The same technique of thick section preparation was applied for air bubble and

air hydrate studies. Thick sections were cut along the core axis that represented continuous 9-cm increments of the core length (4 to 40 years' accumulation, depending on depth). The upper and lower surfaces of each thick section were microtomed and then polished with a small amount of alcohol. Silicone oil was applied to avoid air between the ice slice and the glass plate to which it was attached with supercooled water drops, as well as to prevent sublimation from the upper surface of the slice. The thickness of the thick sections was kept at about 2–4 mm during inclusion-size measurements, and then thinned down to 1–2 mm before counting the number of inclusions. The thick sections were analyzed under a binocular microscope in the field laboratory at $-10\text{ }^{\circ}\text{C}$.

Ensembles of air inclusions in ice (see Fig. 1) were treated in our study as polydispersed systems of spheres uniformly distributed in space. The size distribution function and the number concentration of spheres determine geometrical properties of such systems [35]. For polar ice, the size of each inclusion is expressed by the radius r of an equivalent sphere: $r = \sqrt[3]{(3/4\pi)\nu}$, where ν is the inclusion volume. If a distribution of the inclusions obeys the log-normal law their ensemble can be described by three parameters: the mean value, $\langle \ln r \rangle$, and the variance, $\sigma_{\ln r}^2$, of the variable $\ln r$, and the number concentration of inclusions N . The following statistically exact relationships hold for a random sample of the inclusion radii:

$$\langle \ln r \rangle = \ln \langle r \rangle - 0.5\sigma_{\ln r}^2,$$

$$\sigma_{\ln r}^2 = \ln \left[1 + \left(\frac{\sigma_r}{\langle r \rangle} \right)^2 \right],$$

where $\langle r \rangle$ and σ_r are the arithmetic mean and the standard deviation of the inclusion radius r , respectively.

In practice, when measuring the size of an air inclusion under an optical microscope, either a spherical or a cylindrical visual approximation of the inclusion (depending on its real shape) is used to estimate equivalent-sphere diameter D . For elongated inclusions (cylindrical approximation) this can be $D = \sqrt[3]{(3/2)x_1^2x_2}$, where x_1 and x_2 are the average shorter and longer dimensions of the inclusion, respectively. A measurement requires the aid of the linear scale built into the microscope eyepiece, but to obtain reliable data on inclusion-size distribution, the microscope's magnification should be adjusted to allow the biggest inclusion to measure up to 20–30 scale units [36]. Following this rule, the magnification (length of a scale unit) during routine measurements was progressively changed from $20\times$ (0.05 mm) for air bubbles in the upper section of bubbly ice to $100\times$ (0.01 mm) for air bubbles in the transition zone and for air-hydrate crystals. Thus, inclusions up to those 0.01-mm in diameter could be lost from the experimental size distributions in the routine mode of observations. Before interpreting the experimental data it is important to realize that the overall systematic error of a single D (or r) measurement, including the absolute error of eyepiece scale ($\pm 5\%$) and an individual error of an operator in visual approximation procedure, could be as large as 10%.

At least 200 inclusions were measured in each thick section to obtain statistically representative data on their size distribution. The shapes of the inclusions were recorded simultaneously with their sizes. To avoid

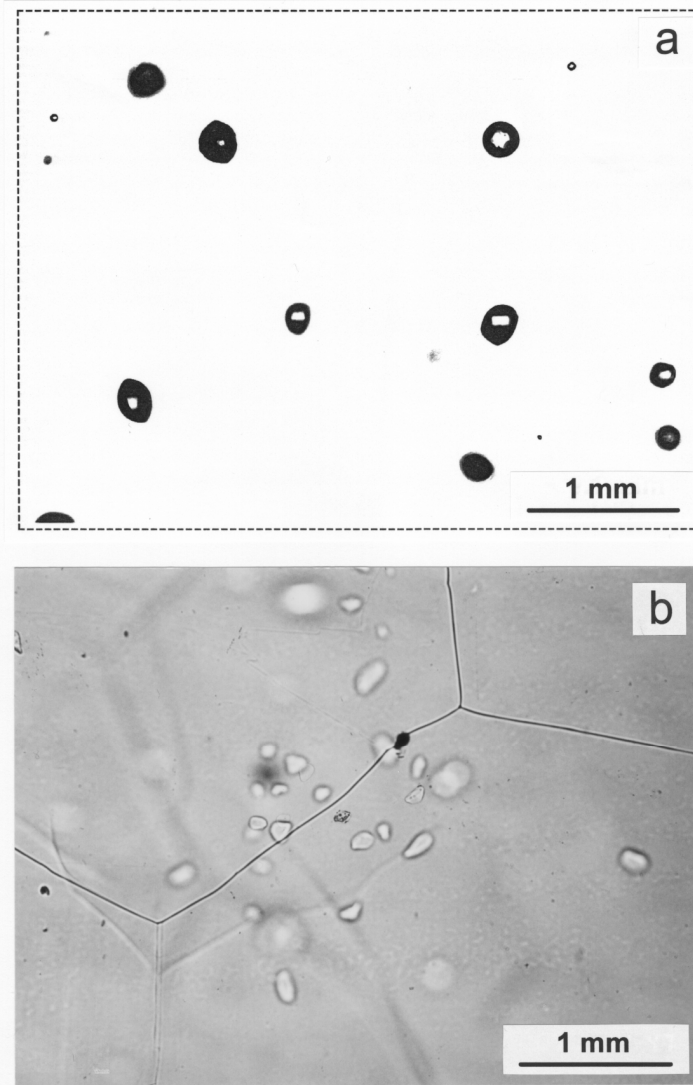


Figure 1: Air inclusions in the fresh Vostok ice core: (a) “Normal” bubbles and microbubbles in ice recovered from a depth of 250 m. (b) A group of air clathrate-hydrate crystals (2500 m).

misinterpretation of the bubble shapes, which can rapidly change in the thick section at $-10\text{ }^{\circ}\text{C}$, control observations were regularly carried out on thick specimens of ice immediately after their extraction from the drill core barrel.

The number concentration N of inclusions was measured in the same thick sections, but used a lower magnification of

the microscope. The procedure consisted of counting the number of inclusion within a calibrated field of vision. A total of 200 to 800 inclusions were counted in 20–40 separate fields of vision randomly distributed over each thick section. The thickness of a thick section was measured at several points by means of an optical microscope. The number of inclusions per

unit mass of ice (N) was then calculated based on the results of the measurements and the density of ice. An overall systematic error of the measurements of N was estimated to be within $\pm 5\%$; the main contribution to the total error came from the thickness measurement ($\pm 3\%$).

To estimate the total uncertainties resulting from both the natural short-term variability of the inclusion characteristics and the random experimental errors, the size and concentration measurements were recorded separately for each of the four successive 2–2.5-cm ice layers represented in each 9-cm long vertical thick section. The variability of the mean radii $\langle r \rangle$, equal to the standard deviation from the mean value for the whole thick section, was about 6–7% for air bubbles and air hydrates, whereas the variability of the number concentration N averaged 8% for bubbles and 18% for hydrates. The value for hydrates is larger because the non-uniformity of the spatial distribution of air hydrates is greater than that for air bubbles (see subsection 4.1 below).

The average reproducibility of the measurements, estimated by comparing results from different thick sections cut from the same horizontal layer of ice core, was found to be about 4–5% for size and concentration measurements on both types of inclusions. Summarizing, the experimental procedure used for the thick-section analysis was appropriate with respect to the natural properties of the inclusions studied and the expected systematic errors of the direct measurements involved.

Because of the common shape of the inclusion-size distributions, a log-normal distribution function has been chosen to fit the data [13, 17], and then the total volume of air inclusions, V , in a unit mass of ice

can be obtained from the following relation [36]:

$$V = \frac{4}{3} \pi \langle r \rangle^3 k^3 N, \quad (1)$$

where

$$k = e^{\sigma_{\ln r}^2} = 1 + \left(\sigma_r / \langle r \rangle \right)^2.$$

Note that in Eq. (1) $\langle r \rangle_{k=\bar{r}}$ is the radius of a mean-volume inclusion defined so that

$$\frac{4}{3} \pi \langle \bar{r} \rangle^3 = \langle v \rangle.$$

Estimates of V using Eq. (1) were shown to be within a few percent of the volume concentrations calculated from the experimental volume distributions [17]. Regardless of the way of calculation, the absolute error of V resulting from uncertainties in the variables r and N , obtained from direct and indirect measurements, is expected to be up to $\pm 20\%$ (assuming 5% systematic errors in both N and r) or $\pm 35\%$ (assuming a 10% error in radius). The contribution to the overall error from radius-related errors is nearly 80% in the first case and nearly 90% in the second.

2.2. Data reconciliation

Hereafter subscripts “b” and “h” will denote characteristics of bubbles and hydrates, respectively, and subscript “s” will denote the state of air at standard conditions (STP, i.e., $T_s = 273.1$ K, $P_s = 0.1013$ MPa).

The volume concentrations of air bubbles (V_b) and air hydrates (V_h) are related to the density ρ and air content V_s of polar ice. Neglecting the mass of air occluded in ice, V_b is related to the ice density by

$$V_b = \frac{1}{\rho} - \frac{1}{\rho_i}, \quad (2)$$

where ρ_i is the density of pure ice. In the bubbly ice stratum the volume concentration of air bubbles is proportional to their air content V_{bs} :

$$V_b = \frac{d_s}{d_b} V_{bs} = z \frac{T_b P_s}{T_s P_b} V_{bs}, \quad (3)$$

where d_s and d_b are the densities of air at STP, and at the current temperature (T_b) and pressure (P_b) in the bubbles, respectively. The factor z is the non-ideal compressibility coefficient of air, which changes from $z = 1$ in the bubbly ice to $z = 0.9$ – 0.95 in the transition zone [26, 37]. The air content V_{bs} is the volume of dry air in the bubbles at STP per unit mass of ice.

Air clathrate-hydrate crystals contain air molecules engaged in the host lattice with crystallographic structure II [4]. The relation between the volume of hydrate crystals in a unit mass of ice (V_h) and the amount of air stored in these crystals (V_{hs}) is given by Uchida and others [13]:

$$V_h = \frac{d_s}{d_h} V_{hs} = \frac{N_L a^3}{n \alpha} V_{hs}, \quad (4)$$

where $N_L = 2.69 \cdot 10^{19} \text{ cm}^{-3}$ is the Loschmidt's number, and d_h is the density of air molecules in hydrate. The latter is

determined by crystallographic parameters of air hydrate: the lattice constant, $a = 1.72 \cdot 10^{-7} \text{ cm}$; the number of cages in a unit cell, $n = 24$; and the cage occupancy α for which a value of 0.90 ± 0.05 is taken as the best estimate based on the recent X-ray and neutron diffraction works [38, 39].

Using Eqs. (2)–(4) one can compare the results from the thick-section analyses with independent, more accurate data on density (porosity) and air content of ice.

In the upper 2546-m section of the Vostok core, the total air content of ice (V_s) was measured using three different analytical techniques with calibration based on the most accurate data from vacuum-volumetric method (absolute accuracy better than $\pm 1.5\%$) [28, 29]. The recent extension of the air content record down to the bottom of the Vostok core was done using a new barometrical method ($\pm 0.6\%$) [40]. In both data sets, the ice was sampled from the same depth levels for both air content and thick-section studies. In the depth interval of 1500–3310 m (i.e., well below transition zone), the air contents V_{hs} calculated using Eq. 4 from the results of air hydrate measurements were systematically 8.5% lower than the values obtained from the gas extraction techniques.

Bubble volume concentrations deduced from the results of the thick-section measurements were 25% lower than V_b values calculated from ice densities obtained by hydrostatic weighing (absolute accuracy is $\pm 0.01\%$ for the density) of unfractured ice samples from the 120–250-m depth interval [30].

Based on the above consideration of the possible systematic errors associated with microscopic measurements, the observed discrepancies are not surprising. Most likely they are caused by a scale-

related error in the inclusion size determination. Thus, the scaling factor to correct the air-bubble and air-hydrate radii can be established under reasonable assumption that $V_s=V_{bs}$ above the transition zone and $V_s=V_{hs}$ below it. The scaling factor was calculated to be 1.10 for the air-bubble measurements and only 1.03 ± 0.02 (at $\alpha = 0.90 \mp 0.05$) for the air-hydrate measurements. The difference is attributed mainly to the different resolutions of the microscopes used.

The corrected data are presented in Fig. 2 in which the vertical bars shown for the inclusion concentrations and mean radii indicate standard deviations of the values obtained in the four 2–2.5-cm layers within each 9-cm long thick section.

3. Air bubbles

3.1. Two generations of bubbles in Vostok ice

A major portion of atmospheric air in polar ice is occluded during pore closure, which takes place at Vostok between 90 and 105 m below the surface. Further evolution of the trapped bubbles in a sinking ice layer results essentially from post-closure disintegration (break-up) of the cylindrical inclusions and compression of all bubbles in plastically-deforming ice matrix driven by the pressure drop between the two phases. The disintegration is complete at 170 m, below which depth the ensemble of air bubbles in ice progressively approaches a polydispersed system of spheres (see Fig. 1a). Bubble elongation does not occur at Vostok because of insufficient strain rate [41].

Besides the “normal” bubbles formed in the close-off zone, a significant number

of microbubbles entrapped by ice grains growing by sublimation-condensation mechanism in snow and between grains in the shallower section of firn have been detected in the Vostok core. Microbubbles (see Fig. 1a) are clearly distinguished from normal bubbles by their smaller size, smoothed spherical surface, and preferable location in the interior of ice crystals down to at least 350–400 m; they can be easily traced in the deeper ice until the conversion of air bubbles to hydrates becomes visible at 600–700 m.

Existence of these two generations of air bubbles in ice manifests itself in the experimental number-by-size distributions and in the results of bubble-pressure measurements. A representative example of bubble-size distributions obtained at a depth of 183 m, where identification of microbubbles is obvious, is shown in Fig. 3. $F(r_b)$ is defined here as

$$F(r_b) = \frac{1}{N_b} \frac{dN_b}{dX},$$

where

$$X = (\ln r_b - \langle \ln r_b \rangle) / \sigma_{\ln r_b}.$$

The normalized representation was chosen to emphasize similarity in the two distributions. Indeed, despite considerable differences in the mean bubble radii (0.15 mm for normal bubbles versus 0.04 mm for microbubbles), and the bubble number concentrations (380 g^{-1} and 110 g^{-1} , respectively) the relative variance (coefficient of variation) was the same for both populations: $\sigma_{r_b} / \langle r_b \rangle = 0.40$. The probability density functions given by

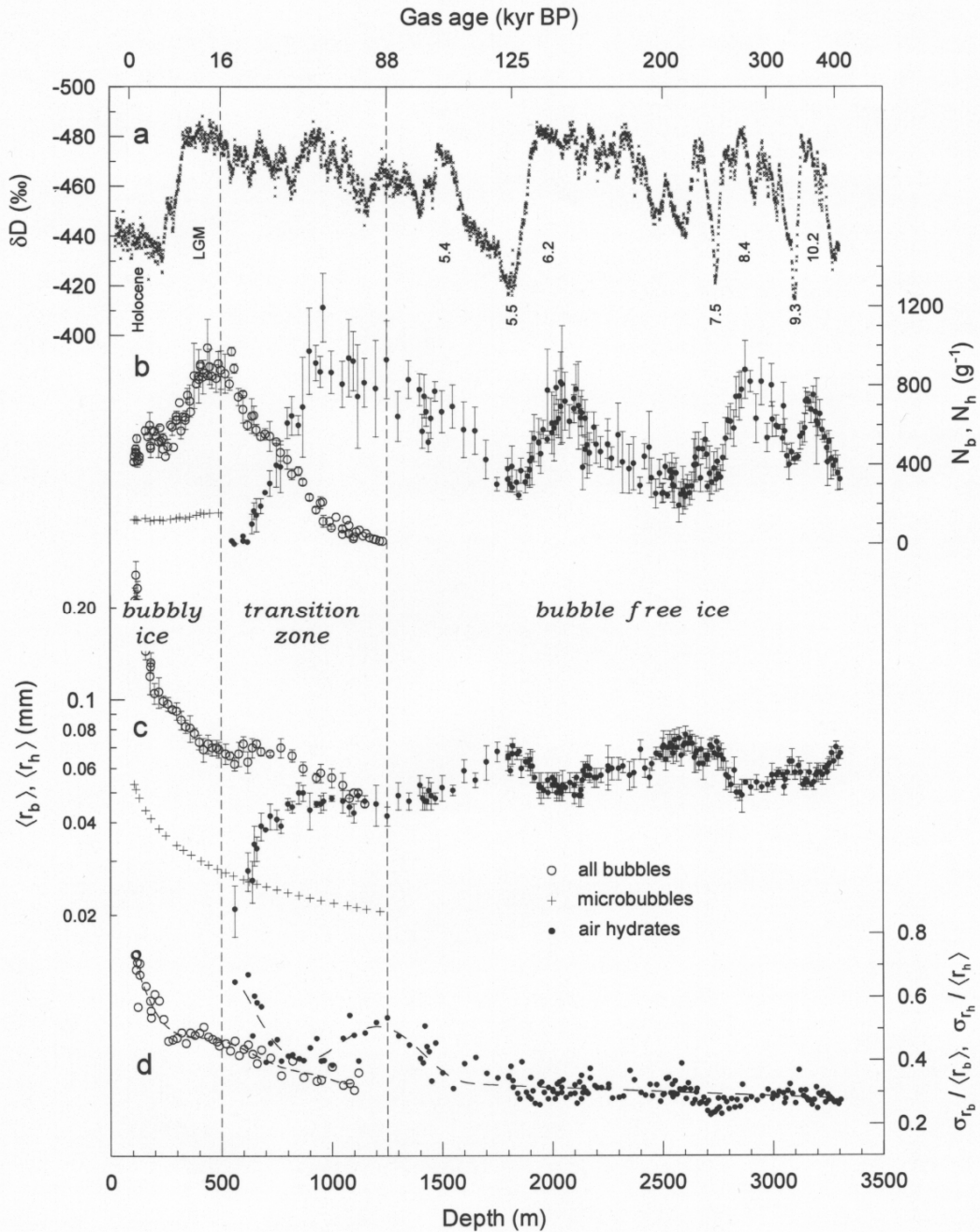


Figure 2: (a) The deuterium record obtained from the Vostok ice core [33]. The marine isotope stages are identified in Ref. 33. The δD axis is inverted, and the depth for each δD value is corrected for the halved difference between the age of ice [20] and the age of the entrapped gas [63] as more appropriate for comparison with experimental profiles of air inclusions. (b) Numbers of air bubbles (N_b) and air-hydrate crystals (N_h) in 1 g of ice. Vertical bars indicate the variability of the inclusion concentration within a 9-cm core increment. (c) Mean radii of air bubbles ($\langle r_b \rangle$) and air-hydrate crystals ($\langle r_h \rangle$). The radii of the microbubbles were calculated from the data on microbubbles from the 183-m depth. (d) Relative variance of the bubble and air-hydrate radii ($\sigma_r / \langle r \rangle$).

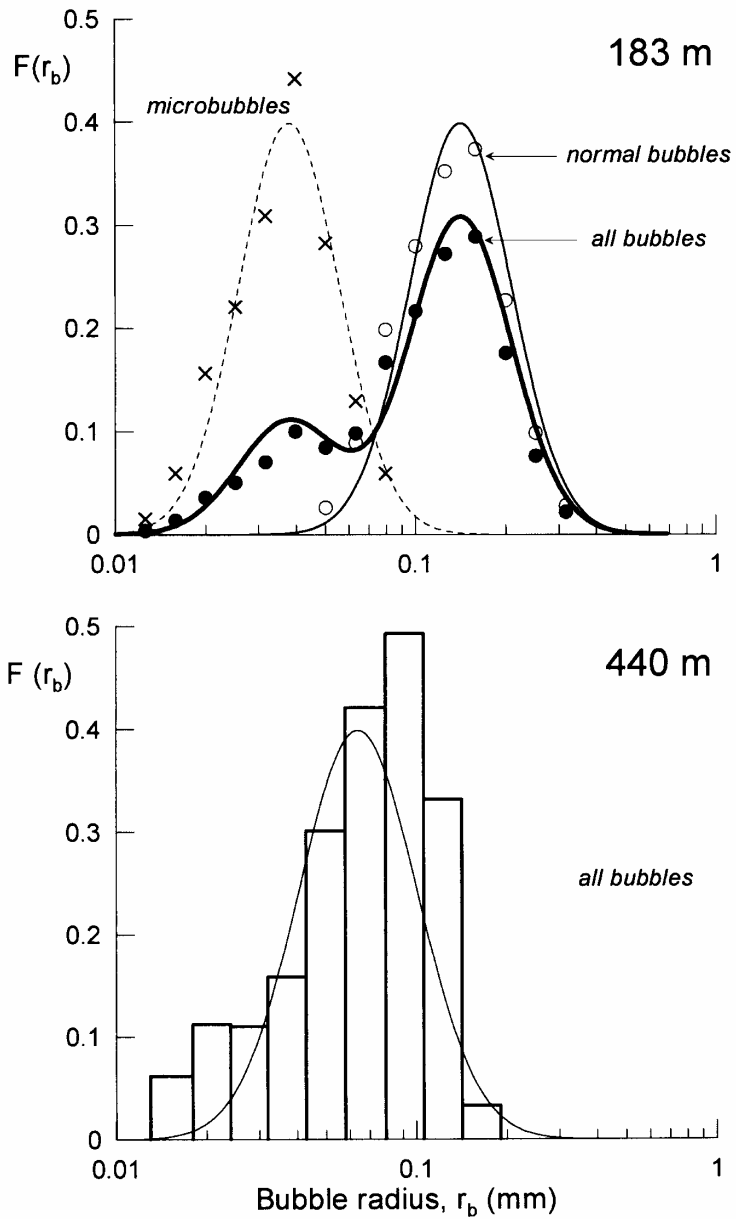


Figure 3: The normalized bubble-size distributions at the 183-m and 440-m depth levels. 183 m: The log-normal functions corresponding to the data on microbubbles (\times) and normal bubbles (\circ) are shown by dashed and solid curves, respectively. The experimental distribution of all bubbles (\bullet) should be compared with the bold curve designating the function $F_{all}(r_b) = q_n F(r_b^{(n)}) + q_m F(r_b^{(m)})$, where $F(r_b^{(n)})$, $F(r_b^{(m)})$ and q_n , q_m are the log-normal distributions and the number fractions, respectively, for both normal bubbles and microbubbles. The total number of inclusions measured in this specimen was 2500. 440 m: Number-size distribution of all bubbles (histogram) determined from measurements of 1200 bubbles. The log-normal distribution is also shown for comparison.

$$F(r_b) = \frac{1}{\sqrt{2\pi}} \exp(-X^2/2),$$

and with parameters taken from the experimental samples are shown in Fig. 3 (183 m) for comparison. The size distribution function for all bubbles (the total-bubble-size distribution shown by the bold curve in Fig. 3, 183 m) was constructed as a weighed mean of the two log-normal functions: $F_{all}(r_b) = q_n F(r_b^{(n)}) + q_m F(r_b^{(m)})$, where $F(r_b^{(n)})$, $F(r_b^{(m)})$ and q_n , q_m are the log-normal distributions and the number fractions of the normal bubbles and microbubbles, respectively.

A more detailed study of the bubble-size distributions [32] shows that between 170 and 500–600 m in the Vostok core both bubble generations are characterized by the same steady-state distribution of relative radii with the same relative variance of about 0.40. Small fluctuations around this value reveal only little climate dependence in the case of normal bubbles.

The bimodal shape of the total-bubble-size distribution is particularly distinct in the upper section of bubbly ice, and tends to develop with depth towards a log-normal-like pattern. However, it stabilizes below 250 m at some intermediate state as the pressure in the normal bubbles approaches that in microbubbles in the asymptotic phase of bubbly-ice densification [37]. This steady state of the total-bubble-size distribution causes the relative variance to remain nearly constant at 0.48 ± 0.03 for all bubbles within a depth interval of 250–500 m (see Fig. 2d). As a result, on the threshold of the bubble-hydrate transition the total-bubble-size distribution deviates noticeably from the log-normal law (Fig. 3, 440 m).

3.2. Bubble pressure

The different origins of normal bubbles and microbubbles is supported by direct measurements of gas pressure within individual inclusions. These were performed using the experimental procedure suggested by Scholander and Nutt [42] and further developed by Gow and Williamson [43], and Lipenkov and others [30]. The pressure in about 100 bubbles was measured at each selected depth level, thus allowing estimates of the mean pressure and dispersion at each depth. The experimental errors of individual pressure measurement varied from about 30% at a pressure of 0.1 MPa to about 5–10% at 2.5 MPa with a tendency to overestimate pressures that exceeded 1 MPa [30]. For each depth, between 10 and 20 measurements of the pressure in microbubbles was also attempted, although the accuracy of these somewhat delicate measurements was less because of the small size and spherical shape of the inclusions.

The results are plotted versus depth in Fig. 4 along with the bubble pressures deduced from accurate density measurements [30] with the (common) assumptions of a constant porosity and atmospheric pressure at the close-off depth [44]. The discrepancy between the two sets of data on gas pressure in normal bubbles (it is certainly the normal bubbles that governs the density of ice) has been attributed partly to systematic overestimation of pressures that were measured as greater than 1 MPa, and partly to an overestimate of the ice porosity below 250 m because of the fissure effect. Finally, the modeled profile (solid curve in Fig. 4) giving the average values of the pressure as compared to the best fits between the ice densification model and the different data sets, is assumed to equal the

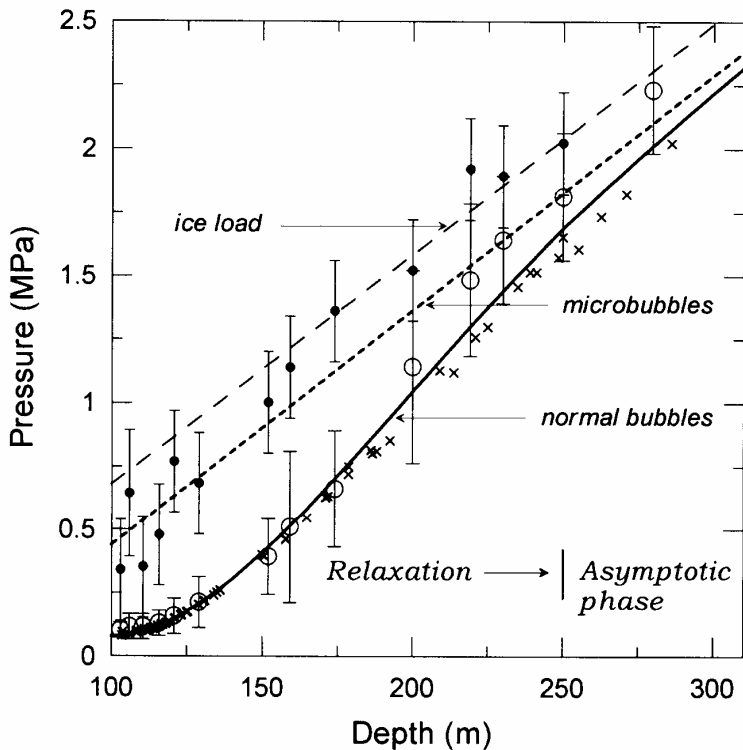


Figure 4: Bubble pressure vs. depth at Vostok. The data are labeled by the following symbols: (○) direct pressure measurements in the normal bubbles (vertical bars indicate a variability of the pressure in the individual inclusions), (●) direct measurements in the microbubbles, and (×) bubble pressures deduced from the accurate ice porosity profile measured using the hydrostatic method. The modeled profile shown as a solid curve should be the most realistic representation of the normal-bubble pressure at Vostok [30]. The pressure curve for microbubbles (dotted line) is obtained as described in the main text.

pressure of normal bubbles at Vostok [30, 37].

Because of the significant bubble-pressure lag (ΔP , the difference between bubble pressure and the absolute load pressure) the shrinking of normal bubbles proceeds rapidly in the relaxation zone of bubbly-ice densification until reaching an equilibrium between the rate of compression and the rate of ice loading (accumulation) approximately 250 to 300-m deep at Vostok (Fig. 4). Further compression of normal bubbles in the asymptotic phase of densification is

governed by a minimal bubble-pressure lag (0.15 ± 0.10 MPa) and controlled by the linear-viscous behavior of the surrounding ice matrix [30].

Significant compression of microbubbles does not occur until the snow-firm transition depth (~ 27 m at Vostok) is reached by a sinking ice particle. The ice load is less than 0.2 MPa at this depth, which means that microbubbles that formed in the shallower part of snow stratum do not possess the relaxation phase of compression. However, the microbubble-pressure lags at the depths within and just

below the close-off zone range from 0.1 to 0.4 MPa with a mean value of 0.25 MPa (see Fig. 4). This implies that some of the examined inclusions were trapped between snow-firn and firn-ice transitions. Finally, the line connecting the modeled value $\Delta P = 0.15$ MPa for normal (all) bubbles at 500 m and experimental estimate $\Delta P = 0.25$ MPa for microbubbles at 100 m (see dotted line in Fig. 4) is thought to be a good approximation of the microbubble pressure in the depth range from 100 to 500 m.

3.3. The climate-related variations of bubble characteristics

The concentration of air bubbles in ice appears to be constant after reaching the end of the bubble disintegration zone. (Ref. 32 has a more detailed discussion of this.) This conclusion is supported by several measurements showing that below disintegration zone the bubble concentration is remarkably constant with depth at stationary (Holocene) conditions [15, 17, 19, 43, 44]. Thus, discovered in the Vostok ice core considerable changes in the bubble sizes and concentrations between the 170 to 286-m (Holocene) and 380 to 500-m (Last Glacial Maximum, LGM) depth intervals (see Fig. 2b, c) have been attributed to a change in the ice formation conditions during the last climatic transition [17]. The number concentration of bubbles was found to be 1.7 times greater in LGM ice than in Holocene ice, whereas the bubble radius in LGM ice averaged only 80% of the expected value for stationary conditions. Because the characteristics of total-bubble populations are determined in the main by those of normal bubbles, it is believed that the above-mentioned climate signal originates primarily from a change in the

geometrical properties of porous firn in the close-off zone (see section 6 below).

Little is known about possible climate-related variations of microbubbles. The abundance of microbubbles measured down to 500 m appears to increase slightly in the LGM ice (see Fig. 2b). The fraction of microbubbles in bubble populations decreases from about 23% to 18% between 170 and 500 m, which could be attributed to increasing uncertainty in bubble type identification with depth. However, the number fractions of microbubbles in the other Holocene ice cores drilled at Komsomolskaya Station (-54 °C) and at the drilling site located 400-km inland from Mirny Station (-40 °C) were found to be 21% and 17%, respectively [31]. Based on these data, we hereafter assume that microbubble concentrations are $20 \pm 5\%$ of the total bubbles in cold polar ice, and that the same 5% level of uncertainty also applies to the identification of bubble types performed down to a depth of 500 m in the Vostok ice core. To avoid excessive cluttering of the graph, the experimental profiles for normal bubbles are not plotted in Fig. 2. The main characteristics of the two generations of bubbles in the Vostok core are summarized in Table 1.

Below approximately 500–600 m, normal bubbles and microbubbles become difficult to distinguish. To estimate the size that microbubbles would have in the bubble-hydrate transition zone if they exist there, we calculated the mean radius-depth profile of the inclusions based on the data from 183-m depth level, and used Eqs. (1) and (3) with fixed values of air content V_{bs} and coefficient of variation $\sigma_{r_b} / \langle r_b \rangle$ as shown in Table 1. The results of these calculations are shown in Fig. 2c. They indicate that the mean size of air hydrates at

Table 1: Summary of data on two types of bubbles in the Vostok ice core.

Air bubble type	Bubble-size distribution (170-500 m)	Mean radius, mm, at 183 m	Relative variance of the bubble radii (170-500 m)	Number fraction*, % (170-500 m)	Volume fraction*, % (≈ air content) (170-500 m)	Pressure lag, MPa, at close-off	Pressure lag, MPa, at 500 m
Normal bubbles	log-normal	0.153	0.40	80	99.7	0.60	0.15
Microbubbles	log-normal	0.040	0.40 [†]	20	0.3	0.25	0.15
All bubbles	bimodal	0.132	0.48 [‡]	100	100	0.53	0.15

*With respect to all bubbles

[†]Value for 183 m

[‡]Value for 250-500 m

the beginning of the transition is much closer to the mean size of the microbubbles than to that of normal bubbles (More discussion of this is in subsection 5.1 below).

4. Air-hydrate crystals

The bubble-hydrate conversion can occur when the bubble pressure is greater than or equal to the dissociation pressure of mixed air clathrate hydrate. According to Miller's diagram [2] this condition is met at Vostok from the 380-m depth [25]. However, the shallowest air-hydrate crystal was found in an ice sample recovered from the 500-m depth [18] when systematic measurements were not yet possible down to 560 m. The presence of bubbles in ice could still be seen with the unaided eye in the fresh ice core down to at least 1400 m, and the last bubbles in the thick sections were found at the 1250-m depth.

4.1. Morphological types of crystals and their prevalence

A number of classifications have been proposed to describe the morphological diversity of air-hydrate inclusions in polar ice sheets [3, 13, 15, 19]. A simplified classification scheme adopted in the present study (similar to that suggested by Pauer and others [15]) is thought to be sufficient in the sense that it refers to the genesis of the inclusions. The morphological descriptions given below are based on microscopic observations of the projected images of air hydrates in the thick sections of ice, as well as on the observations of hydrates that were isolated from ice subjected to an eutectic melting in ethylene glycol. Interestingly, isolated air hydrates could keep their shape while floating in ethylene glycol (at -10 °C and ambient pressure) for a few seconds before their explosive decomposition. This allows the shape and the habitus of the crystals to be correctly identified under a binocular microscope.

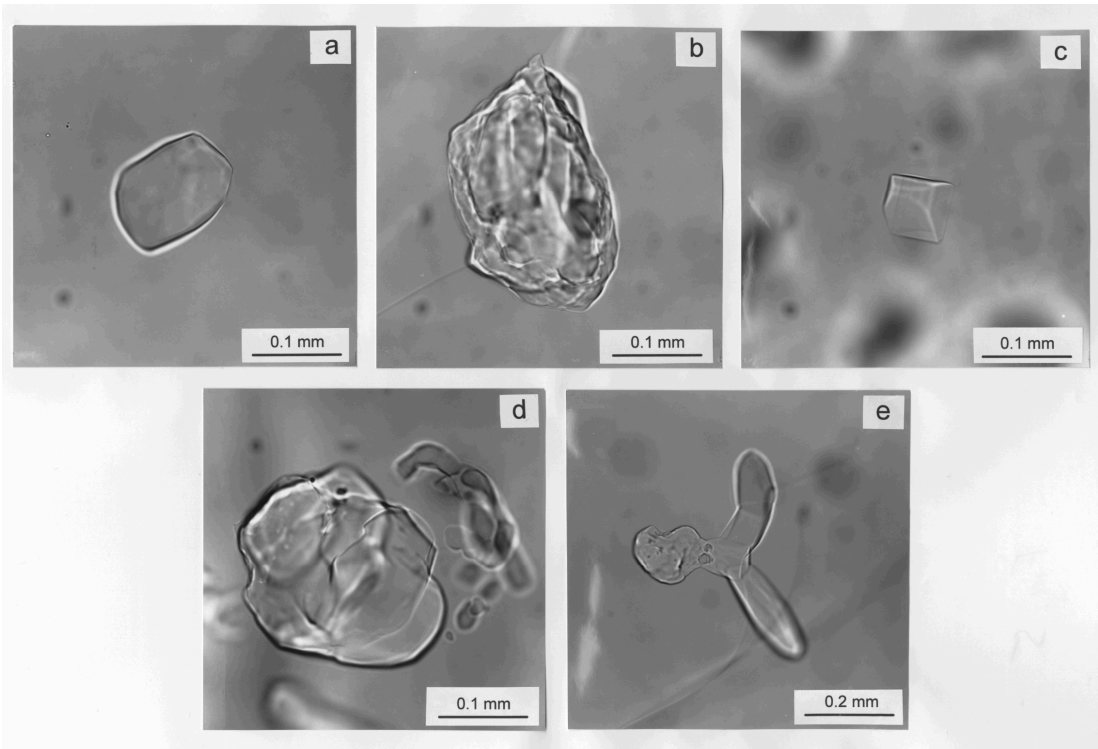


Figure 5: Morphological types of air-hydrate inclusions observed in the Vostok ice core. (a) Rounded crystal. (b) Cloud-like hydrate. (c) Faceted crystal. (d) Collapsed hydrate. (e) Cluster containing several air-hydrate crystals.

Rounded (i.e., spherical [3, 13, 15], oval [13], partly faceted [13], and ellipsoidal [19]) crystals are most common in the Vostok core (see Fig. 1b and Fig. 5a). Their number fraction with respect to the whole population of hydrates ranges from 70 to 98%. A typical size of the crystals expressed by equivalent-sphere radius is about 0.06 mm. These monocrystalline inclusions are thought to be formed by one of the two proposed types of bubble-hydrate conversion [26, 45]: concentric and linear growth of a clathrate nucleated at the bubble-ice interface (see Fig. 10 in the paper by Kuhs and others, this volume). Slow post-conversion growth at low supersaturation could account for the near-equilibrium form of these crystals.

The cloud-like (i.e., graupel-like [3] and irregular [13, 15, 19]) hydrates shown in Fig. 5b represent up to 15–20% of all clathrates in the transition zone but completely disappear below 3000 m (see Fig. 6b). Their typical size is ~ 0.09 mm. Morphological features of the cloud-like inclusions are nearly the same as those of the “recovered” clathrates that were grown from secondary (nucleated) air cavities in the Vostok ice samples pressurized at 18 MPa [45, 46]. Thus, the concentric growth from single or several nuclei observed in the laboratory experiments could be also expected in the case of cloud-like hydrates growing from large, supersaturated air bubbles in ice sheets. The apparent disappearance of these shapes below 3000 m

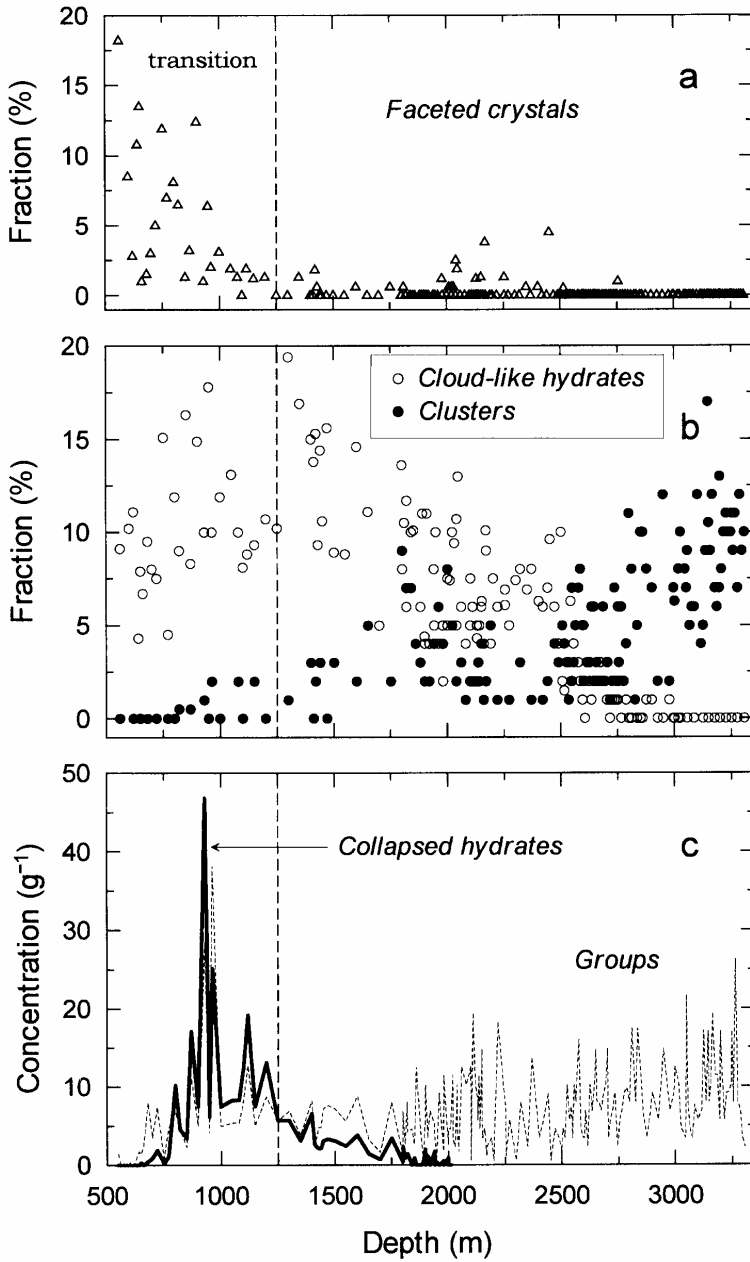


Figure 6: (a) Number fraction of faceted crystals. (b) Number fractions of cloud-like hydrates and clusters. (c) Number concentrations for the collapsed hydrates and the hydrate groups.

probably results from surface smoothing in the course of diffusive spheroidization that is driven by the Gibbs-Thomson gradient of air-molecule concentration in ice matrix near the hydrates.

The faceted (i.e., triangular [3], hexagonal [3], tetrahedral [3], and polyhedral [3, 13, 19]) crystals shown in Fig. 5c are found mainly in the transition zone (see Fig. 6a). The small size of these

crystals (~ 0.035 mm) suggests their parentage from small (micro-) bubbles, and their regular crystallographic shaping (kinetic growth form) points out the role of post-conversion crystal growth sustained by air-molecule fluxes from neighboring supersaturated air bubbles: the mechanism described earlier by Hondoh [23, 24]. Therefore, an enrichment of oxygen in hydrates at the beginning of the transition at Vostok [12, 16] is expected to be larger in these crystals. The rapid disappearance of faceted crystals below the transition in the course of air-hydrate coalescence might be attributed to their enhanced "solubility" in ice due to their small size and specific gas composition.

The number fraction of "rod-like" (i.e., elongated [15] and long-rod [19]) hydrates (not shown in Fig. 5) described by Uchida and others [13] does not exceed 5% in the Vostok core. These, generally two-dimensional lamellate inclusions, which do not reveal the presence of air during their treatment with ethylene glycol, certainly deserve deeper investigation, which will be presented elsewhere.

The term "collapsed hydrate" will be used to designate a compact group of several splinter-like hydrates partly assembled in polycrystalline aggregates (Fig. 5d). The formation of such groups has been attributed to the possible destruction of a growing hydrate shell in the course of bubble-hydrate conversion [26]. Because of the high supersaturation of bubbles, immediately after nucleation a considerable amount of air (30–60%) converts to hydrate. The resulting pressure drop causes rapid compressive deformation of both the surrounding ice and the confined hydrate shell, thus making it possible for the shell to collapse. The concentration of collapsed

hydrates reaches a maximum in the middle of the transition zone (see Fig. 6c), and then decreases with depth. Below 2000 m, merging (coalescence) of these collapsed hydrates results in their apparent disappearance.

Unlike air-bubble ensembles, the air-hydrate inclusions in Vostok ice are often characterized by a nonuniform spatial distribution (see Figs. 1a and b). One possible explanation for this is that the hydrates migrate along with grain boundaries in ice. This hypothesis is supported by the observations that grain growth occurs at Vostok over the depth range under consideration [47, 48], that air hydrates at least down to 2500 m are more frequent on the grain boundaries [49], thus hampering their migration [50], and that the groups with enhanced concentration of hydrates are more frequent in the vicinity of grain boundaries than in the interior of ice crystals (see Fig. 1b). In addition, a type of self-perpetuating mechanism of hydrate clustering based on their ability to migrate in ice due to nonuniform distribution of air molecules in the surrounding ice matrix [24] could also occur. Whatever the mechanism, the scale of this process is too small to affect significantly averaged results of thin-section measurements and routine gas analyses. The typical size of the air-hydrate groups is about 1 mm, whereas the distance between them is about 5 mm; the concentration of inclusions in groups is about 10 times as high as their mean concentration in the ice matrix. The concentration of the groups themselves has a slight tendency to increase with depth as shown in Fig. 6c.

Clusters assembled of two to ten air-hydrate individuals (see Fig. 5e) appear in the ice as a result of air-hydrate migration

and collision. These polycrystalline inclusions readily disintegrate into separate crystals while being isolated from ice in ethylene glycol. The number fraction of clusters increases with depth up to 10–15% in the bottom section of the core (see Fig. 6c).

As far as the relation between geometrical properties of air bubbles and air hydrates is concerned, one of the important implications of the above morphological study is that collapsed hydrates and individual crystals assembling into clusters should be categorized as single inclusions. The experimental profiles of air-hydrate characteristics shown in Fig. 2b–d satisfy these conditions.

4.2. Geometrical properties of air-hydrate crystals

A striking feature in the air-hydrate record below the transition zone is that the number concentration of crystals (see Fig. 2b) retains approximately the same average level, and varies with the climate with approximately the same amplitude as the concentration of bubbles does above the transition (see also Table 2). This was the first, and remains the most convincing argument that the ratio of the number of succeeding hydrates to that of the preceding bubbles is nearly unity; other arguments are presented in section 5 below. The climate-related variations of the crystal size and abundance retain the sense of the bubble variations: more inclusions of smaller sizes are observed in the glacial-age strata, whereas fewer inclusions of larger sizes are observed in the interglacial-age strata. The results of clathrate measurements performed in the field on unrelaxed ice cores [21] (Fig. 2b–d) are in good agreement with

earlier published data for the depth interval of 1005–2542 m [13].

As shown in Fig. 2d, the relative variance of hydrate radii, after certain excursions within and just below the transition zone, becomes nearly constant ($\sigma_{r_h}/\langle r_h \rangle = 0.30 \pm 0.03$) from about 1500 m to the bottom of the core, showing only a small tendency to decrease with depth. Before analyzing the changes that geometrical properties of air inclusions undergo in the transition zone, it is instructive first to consider the steady-state size distribution of air hydrates within this 1500–3310-m depth interval, which spans about 300 kyr (in terms of gas age).

The stacked air-hydrate-size distributions corresponding to different climatically-steady time periods are shown in Fig. 7a, b. Each stack is based on a number of experimental size distributions with similar parameters that were selected from a depth interval formed under stationary conditions as indicated from the deuterium record [33] (Fig. 2a). Interestingly, unlike the size distribution of all bubbles on the threshold of bubble-hydrate transition (see Fig. 3b), the sizes of the air hydrates, except possibly at the 1425-m depth, can be readily interpreted in terms of log-normal distribution. The relative variance of hydrate radii is almost insensitive to climatic conditions: its average ranges from 0.31 in the interglacial ice strata to 0.29 in the glacial strata.

4.3. Coalescence of air-hydrate crystals in ice

The growth of air-hydrate crystals in ice matrix, which is called coalescence [51] in the present study, is closely related to the diffusive mass transfer between crystals. The latter is driven by the gradients of air-

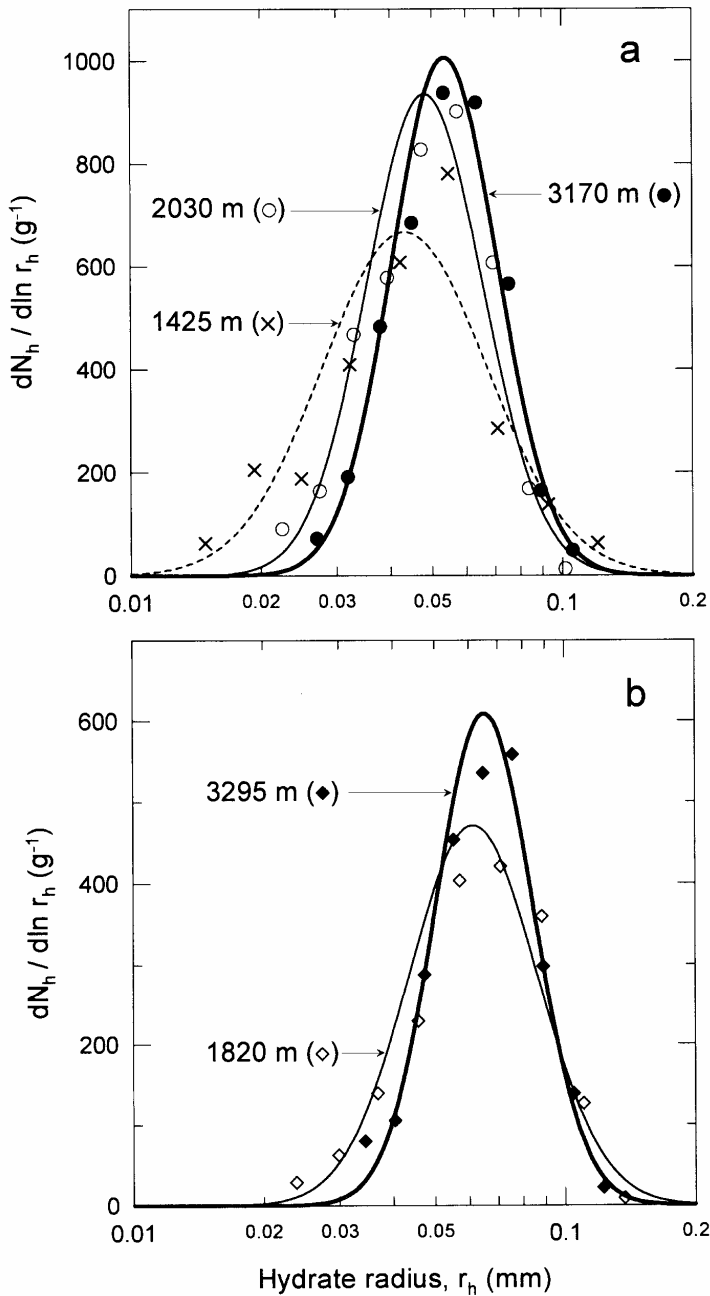


Figure 7: The stacked air-hydrate-size distributions for different climatic periods. (a) The distributions corresponding to the cold (glacial) isotope stages: 1425 m (isotope stage 5.4; gas age 105 kyr), 2030 m (6; 135 kyr), and 3170 m (10; 345 kyr). (b) The distributions corresponding to the warm (interglacial) isotope stages: 1820 m (5.5; 125 kyr), 3295 m (11; 405 kyr). For each case, a number of experimental distributions selected around the designated depth level were used to construct a stacked distribution based on ~ 1000 inclusions. The log-normal distribution functions are shown for each depth level as indicated in the figure.

molecule concentration in ice that exist due to the difference in gas composition of air hydrates [16] and the difference in crystal size (surface curvature) [14, 24].

Following the evolution of the stacked size distributions of hydrates with depth (age) in Fig. 7 one could reveal a tendency of larger crystals to increase in number at the expense of smaller ones. The linear regression between crystal size and the gas age over the depth range 1500–3310 m, although not statistically significant ($R^2 = 0.005$), does show that hydrates tend to grow. Neglecting the difference between an increment of the gas age and the real time span of the growth process the average growth rate is calculated to be $3.7 \cdot 10^{-13} \text{ cm}^3 \text{ yr}^{-1}$ in mean crystal volume. This value is one order of magnitude smaller than the previous estimate of $6.7 \cdot 10^{-12} \text{ cm}^3 \text{ yr}^{-1}$ reported for 1000–2540 m in the Vostok core by Uchida and others [13, 14]. Moreover, applying the same procedure to the number concentration of hydrates N_h , one would find that N_h increases with age at a rate of $1.7 \cdot 10^{-4} \text{ g}^{-1} \text{ yr}^{-1}$. We thus conclude that in the depth range from 1500 to 3310 m the overall effect of crystal growth is not detectable with the simplified approach used.

Conversely, the rapid increase of the crystal radius $\langle r_h \rangle$ accompanied by the decrease of $\sigma_{r_h} / \langle r_h \rangle$ and N_h observed between 1100–1200 m (end of transition) and 1500–1600 m indicates a faster rate of crystal growth in this region despite the lower temperatures compared to the deeper section of the core described above. This could be explained by the large number of small hydrates, enriched in oxygen, which still exist at the bottom part of the transition zone. These small crystals serve as a sink for air molecules (chiefly oxygen) while a

sufficient number of bubbles remain in the nearby ice [12, 24], but they become a source of air molecules for the larger crystals when the bubbles disappear at the end of the transition zone [16]. During a short transient period of coalescence (1100–1500 m) a significant fraction of hydrates that have been converted from small (micro-) bubbles rapidly dissolve in ice matrix to supply the larger, growing crystals with air. (Compare the size distributions for 1425 m and 2030 m in Fig. 7a.) This could partly explain the faster growth rates deduced from the data that include measurements between 1000 and 1500 m [14].

Likewise the normal bubbles after disintegration, after the transient stage of coalescence, the air hydrates attain a fixed distribution of relative sizes ($\sigma_{r_h} / \langle r_h \rangle = 0.30$) which can be approximated by a log-normal function. In the subsequent asymptotic phase of coalescence [51] (1500–3310 m), crystal growth at Vostok proceeds at a low rate that can hardly be recovered from the data unless the climate signal is properly filtered out from the experimental profiles.

However, the coalescence of air-hydrate crystals in the Vostok ice is expected to reactivate at the elevated temperature in the deeper strata of ice sheet, that is, from 3310-m down to 3538-m depth, the interface between glacier and accreted ice [52], where only four degrees in temperature separate ice from the pressure melting point [53]. Significant crystal growth traced throughout the GRIP core [15] (where ice is on average only 10 °C warmer than between 1500 and 3310 m at Vostok) probably refers to the coalescence-temperature dependence.

5. Bubble-hydrate transition

The main features of the bubble-hydrate transformation in ice sheets, as determined from ice core studies, laboratory experiments, and theory can be summarized as follows.

1. Heterogeneous air-hydrate nucleation is the rate-limiting step of the transformation, and it explains the thick transition zone in ice sheets [12, 24, 25, 45, 54]. The probability of nucleation increases with the excess pressure (supersaturation of bubbles) [24, 55] and with temperature [24, 39]. Nucleation of smaller bubbles is favoured [18].
2. The air concentration in bubbles during clathration in cold ice is not sufficient to fill up a bubble with hydrate entirely ($r_h/r_b < 1$) [24], which implies an increase of the ice-densification rate in the transition zone [56]. The compressive deformation of the ice-hydrate-bubble system is a rate-limiting process of the bubble-hydrate conversion [25, 26]. The post-nucleation conversion proceeds rather fast [25, 45, 46] and takes not more than 30 to 400 years in the middle of the transition zone at Vostok [26].
3. Selective diffusion (air-mass exchange) between coexisting bubbles and hydrates [24] results in both extreme gas fractionation [12, 16] and growth of air-hydrate crystals [26]. Also, the dissolution of small crystals in favor of larger ones [14, 16] can affect the properties of hydrates in the post-conversion period.

In general, all the above-mentioned phases of the transformation (nucleation, post-nucleation conversion, and post-

conversion crystal growth) occur simultaneously throughout the transition zone. We now focus on what happens to the geometrical properties of air inclusions as the bubble-hydrate transition proceeds.

5.1. Microbubbles in the transition zone

Because the ice stratum in which the transition occurs at Vostok was formed under relatively steady climatic conditions (see Fig. 2a), one may follow the evolution of the bubble and hydrate ensembles across the transition while assuming their initial properties are constant.

Fig. 8 shows the experimental size distributions of air bubbles and air hydrates at the beginning (640 m) and close to the end (930 m) of the transition zone at Vostok. The reconstructed size distributions of the bubbles that have already been converted to air hydrates at the shallower depths (dotted-line histograms in Fig. 8) were obtained as follows. The radius of a newly formed hydrate (r_h) is related to that of the preceding bubble (r_b) as

$$r_h = r_b \sqrt[3]{\frac{d_b}{d_h}}, \quad (5)$$

where the ratio between the air densities in the bubble (d_b) and in the hydrate (d_h) can be obtained from Eqs. (3) and (4). Neglecting a possible post-conversion evolution of air hydrates, the radii of the preceding bubbles were calculated from the measured radii of hydrates using Eq. (5) and present-day conditions (T_b , P_b) averaged over the depth intervals 560–640 m and 560–930 m. (The depth of 560 m was chosen as the threshold for air-hydrate occurrence in Vostok ice in a systematic way.) The maximum errors of such

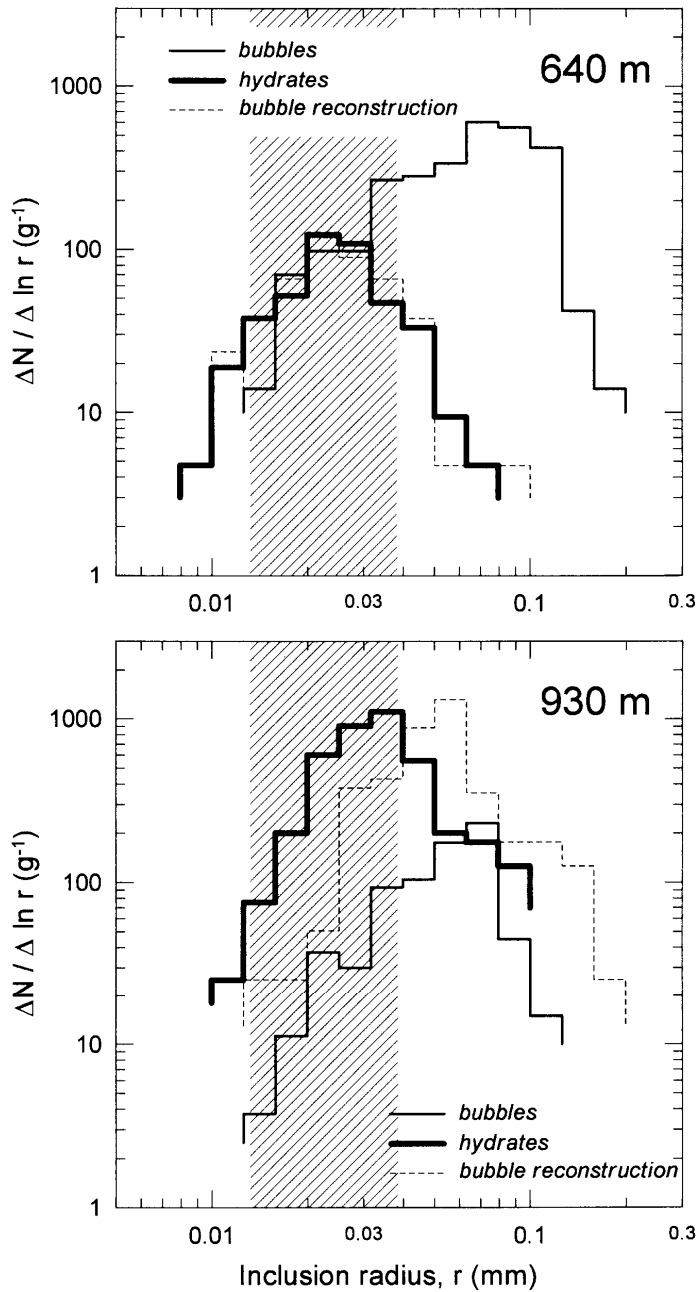


Figure 8: Number-size distributions of air bubbles and air-hydrate crystals at the top (640 m), and at the bottom (930 m) of the transition zone. Each of the histograms is based on measurements of 200 inclusions. The shadowed area indicates the log-normal “ 1σ ” interval for microbubbles calculated so that at least 68% of the log-normally distributed microbubbles would be within this size interval at the pressures and temperatures prevailing in the depth range from 600 to 930 m. The size distributions of the bubbles that have already transformed to air-hydrates (dashed-line histograms) are reconstructed using the experimental hydrate distributions (bold-line histograms) as described in the main text.

reconstruction caused by bubble pressure changes within the averaging intervals are 3% and 10% for the cases 640 m and 930 m, respectively. Note that a possible influence of post-conversion air-mass exchange would tend to decrease the sizes of preceding bubbles.

The shaded region in Fig 8 indicates the expected size range of microbubbles determined as log-normal “ 1σ ” interval:

$$[\exp(\langle \ln r_b \rangle - \sigma_{\ln r_b}); \exp(\langle \ln r_b \rangle + \sigma_{\ln r_b})].$$

Based on the data from 183 m reduced to the bubble pressures at 560 m and 930 m for the upper and lower bounds, respectively, this interval is between 0.013 mm and 0.037 mm. Thus, at least 68% of the microbubbles, if they exist between 560 and 930 m, would be within this size interval.

Although the above approach is oversimplified, it is sufficient to demonstrate that an important fraction (>70%) of the clathrates observed at the beginning of the transition (640 m) were converted from gas inclusions of the microbubble-size range. As the bubble supersaturation increases and the small bubble disappear with depth, the mode of the reconstructed (converted) bubbles shifts towards larger values of r_b , so that at the end of transition (930 m) all remaining (normal) bubbles have entered the size interval of conversion. Straightforward interpretation of these data suggests that probability of nucleation depends on both the excess of pressure and the size of the bubbles.

However, the role of bubble size in clathrate nucleation is not well understood yet. The probability of nucleation should be

proportional to the total area of ice-air interface. The preferential clathration of smaller bubbles, with necessarily larger surface curvature, can be interpreted in terms of higher degree of surface roughness (disordering) that strongly influences the kinetics of clathration [57]. Alternatively, the preferential clathration of microbubbles can be related to their origin, not their size. Indeed, a significant fraction of microbubbles were trapped by ice crystals growing from the vapor in the snow stratum of the ice sheet. The bubble formation in these cases could be associated with high local impurity loading, which could account for easier clathration of such bubbles in the transition zone.

Despite a special effort to find microbubbles with radii less than 0.01 mm in the fresh ice core from the transition zone, none were detected. Thus, a critical bubble size controlled by clathration exists in the transition zone and becomes a lower bound for the size distribution of the shrinking bubble population. This decreases the relative variance $\sigma_{r_b} / \langle r_b \rangle$, and slows the rate of decrease with depth of the mean radius $\langle r_b \rangle$ of the remaining bubbles.

5.2. The link between air-bubble and air-hydrate number-size distributions

At all depths of bubble-hydrate conversion, the volume of a newly formed hydrate is determined by the amount of air in the bubble. If the effects of post-conversion diffusive gas exchange between inclusions are small, then a simple scaling procedure based on Eq. (5) could be used to calculate the resulting size distribution of hydrates from the initial size distribution of all bubbles. Note that such transformation would not affect the relative variance of inclusion radii.

In fact, the average relative variance of the hydrate radii and the average number concentration of the hydrates between 1000 and 1250 m are 0.49 and 850 g⁻¹, respectively, which nearly equal the corresponding mean values of 0.48 and 870 g⁻¹ for the total-bubble populations in LGM ice between 380 and 500 m (see Fig. 2b, d). This observation leads us to an important conclusion: the net effect of the diffusive gas transfer between coexisting bubbles and hydrates is small and undetectable in the available data; however, this gas transfer could affect both the sizes of small hydrates at the beginning of the transition and the sizes of the remaining bubbles (future hydrates) at its end. The excursions of the $\sigma_{r_h}/\langle r_h \rangle$ curve in the upper half of transition zone (see Fig. 2d) can be interpreted in terms of a changing mode of clathrate nucleation: from preferential nucleation in small (micro-) bubbles to random nucleation in all bubbles.

As bubbles disappear at the end of the transition zone, the concentration of air molecules in ice drops to the level determined by the presence of clathrates [12, 16]. The crystal coalescence becomes the main process changing the geometrical parameters ($\langle r_h \rangle$, σ_{r_h} , N_h) of air-hydrate ensembles. To determine the total effect that the bubble-hydrate transformation and subsequent crystal growth have on the number concentration of air inclusions in ice, in Table 2 we compare the average concentration of bubbles and hydrates in the ice strata deposited during four glacial terminations of the past 410 kyr. The averaging intervals for each termination (I–IV) include preceding glacial maxima (LGM, stage 6.2, stage 8.4, and stage 10.2), and subsequent interglacial periods (Holocene, stage 5.5, stage 7.5, and stage

9.3) as indicated in Table 2 and Fig. 2a. Table 2 shows that under similar climates, the number of hydrates in ice amounts to only 80% of the total-bubble number and thus nearly equals the number of normal bubbles above the transition zone.

Summarizing, the data show that by the end of the short transient period of crystal coalescence (~1500 m at present), most of the small hydrates had dissolved in ice to the advantage of the larger, growing crystals. As a result of this process, the number of hydrates returns very nearly the number of normal bubbles as the width ($\sigma_{r_h}/\langle r_h \rangle$) of their size distribution shrinks from 0.49 to 0.30.

To complete the connection between the geometrical properties of air bubbles and hydrates, we have to employ at this step the air content of ice (V_s) which determines the volume concentration of the inclusions. Here we assume that $V_s = V_{bs}$ above the transition zone, and $V_s = V_{hs}$ below it, where V_{bs} and V_{hs} are the air contents of bubbles and hydrates, respectively (see subsection 2.2). We also note that at a given site the V_s , and thus the equivalent-hydrate volume concentration of the inclusions, are substantially constant with respect to the natural variability of the inclusion sizes and number concentrations in polar ice. In case of Vostok, this assertion has been supported by previous [28, 29] and recent (to be presented elsewhere) V_s measurements that show that the air content of ice between 170 and 3310 m remains within $\pm 5\%$ of its mean value.

Given that V_s and $\sigma_{r_h}/\langle r_h \rangle$ are constant, the number concentrations of hydrates are determined from Eqs. (1) and (4) by their mean radii:

Table 2: Mean number concentrations of air inclusions at depth intervals corresponding to glacial terminations.

Climatic period	Depth interval (m)	Inclusion type	Inclusion concentration (g ⁻¹)
Termination I (LGM-Holocene)	170-500	All bubbles	680±155
		Normal bubbles	545±135

Termination II (stage 6.2-stage 5.5)	1720-2140	Hydrates	540±175
Termination III (stage 8.4-stage 7.5)	2702-2910	Hydrates	530±200
Termination IV (stage 10.2-stage 9.3)	3050-3190	Hydrates	575±135
Total for Term II – Term IV		Hydrates	545±170

$$N_h = \frac{3}{4\pi k_h^3 \langle r_h \rangle^3} \frac{d_s}{d_h} V_s. \quad (6)$$

The data on air hydrates are plotted in Fig. 9 along with $N_h(\langle r_h \rangle)$ curve calculated using Eq. 6 at $V_s = 0.0893 \text{ cm}^3 \text{ (STP) g}^{-1}$, and $k_h = 1.09$ ($\sigma_{r_h} / \langle r_h \rangle = 0.3$). The near-perfect fit between the data and the prediction is not surprising given the small (3%) correction of hydrate radii as described in subsection 2.2.

In the case when both the size distribution of bubbles before transition and that of hydrates after transition are fixed, the mean radius of hydrates can be obtained

via Eqs. (1), (3) and (4) from the mean radius of preceding bubbles:

$$\langle r_h \rangle = \langle r_b \rangle \frac{k_b}{k_h} \sqrt[3]{\frac{d_b N_b}{d_h N_h}}. \quad (7)$$

Applying Eq. (7) to the data on normal bubbles from the depth range 170–500 m ($k_b = 1.16$) we derived, at $N_h/N_b = 1$, the mean radii of the potential hydrates log-normally distributed with $k_h = 1.09$. The numbers of normal bubbles plotted against their equivalent-hydrate radii (see Fig. 9) reveal close clustering around $N_h(\langle r_h \rangle)$ curve for real hydrates.

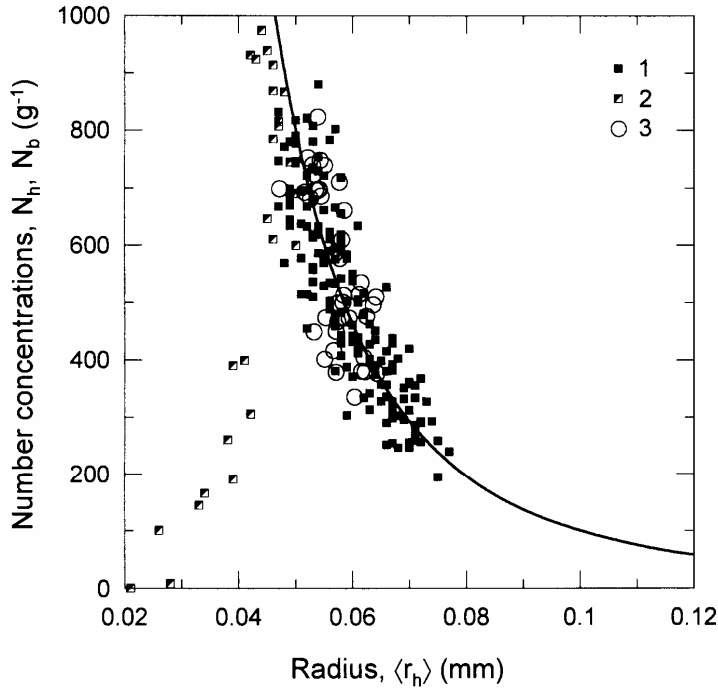


Figure 9: Number concentration N_h of air-hydrate crystals vs. their mean radius $\langle r_h \rangle$. The data on air-hydrates are shown by two types of small squares that designate (1) measurements made below the transition zone, and (2) measurements within the transition zone. The circles (3) designate the number concentrations of normal bubbles plotted against their equivalent-hydrate radii (see text). The solid curve shows the $N_h(\langle r_h \rangle)$ relationship at the constant air content of ice equal to $0.0893 \text{ cm}^3(\text{STP})\text{g}^{-1}$ and the fixed value $\sigma_{r_b}/\langle r_b \rangle = 0.30$ of hydrate-size distributions from the depth interval of 1500–3310m.

However, it is not certain that only the microbubble-related hydrates dissolve and only the normal-bubble-related hydrates grow during the transient period of coalescence. In order to characterize a hypothetical (effective) bubble-size distribution that would reproduce the experimental distributions of hydrates under the condition $N_h = N_b$, the parameters $\sigma_{r_b}/\langle r_b \rangle$ and $\langle r_b \rangle$ were alternately tuned to allow the bubble concentration to fit the $N_h(\langle r_h \rangle)$ curve for real hydrates. The best-fit hypothetical distribution deviates insignificantly from the distribution of normal bubbles: matching is achieved either by a 3% reduction in radius or by reducing the

relative variance from 0.40 to 0.36. Therefore, with the reasonable assumption that air content of ice, relative variance of normal-bubble radii, and that of hydrate radii are invariable, the number-size distributions of succeeding air hydrates can be obtained from the number-size distributions of preceding normal bubbles and vice versa.

Finally, based on the above consideration, we argue that in the asymptotic phase of hydrate coalescence (1500–3310 m at Vostok), the geometrical properties of hydrate ensembles are primarily determined by those of normal bubbles. The climate signal imposed on the

bubble properties at pore close-off is only slightly modified in the resulting number-size distributions of air hydrates which then remain substantially unchanged during a time span of at least 300 kyr.

6. On the origin of the climate signal in the air-bubble and air-hydrate records

A. J. Gow was probably the first to point out that spatial variability of ice porosity at pore close-off in polar ice sheets is small as compared with variability of the ice-grain size and thus “any change in the number of crystals per cubic centimeter at the firm-ice transition should be accompanied by a corresponding change in the number and size of bubbles [44].” More quantitative consideration of this has recently been developed and verified using the new data on air bubbles obtained from the ten ice cores drilled in East Antarctica [22, 31, 32]. In this section, we briefly review the main results of this study as concerns the number of bubbles in ice.

The structure of ice at the close-off depth is approximated by monodispersed system of regular polyhedrons (ice grains) whose dimension can be expressed by the edge length l , or the volume $v = \phi_v l^3$, or the mean projected area $A = \phi_A l^2$ of the polyhedron (e.g., Underwood [35]). The pores are treated as cylindrical channels located along the grain edges and characterized by their radius r_p and total length L_p per 1 g of ice. The number concentration of normal bubbles after their disintegration (N_b) can be written [31]

$$N_b = L_p / \lambda r_b, \quad (8)$$

where $\lambda > 2\pi$ is the criterion of stability of cylindrical bubbles. Then a simple geometrical argument yields the relation between the N_b and the grain size A_c at pore close-off:

$$N_b = \frac{G}{\rho_i A_c^{1.5}} \sqrt{\frac{\rho_c}{\rho_i - \rho_c}}, \quad (9)$$

where ρ_c is the density of ice at the firm-ice transition. The grain size is expressed by the mean projected area of the grains, A_c , through which relations corresponding to other possible measures of size can be readily obtained. The G in Eq. (9) is the morphological factor defined as

$$G = \frac{\sqrt{\pi}}{\lambda} \left(y \frac{\phi_A}{\phi_v} \right)^{1.5},$$

where y is the number of pores per grain, and the values of ϕ_A and ϕ_v are specified by the type of regular polyhedron chosen for ice-grain approximation [35]. Finally, combining Eqs. (1) and (2) one can also derive the relation between the number of air bubbles N_b below disintegration zone and their mean (effective) radius $\langle r_{bc} \rangle$ at pore close-off:

$$N_b = \frac{3}{4\pi k_b^3 \langle r_{bc} \rangle^3} \left(\frac{1}{\rho_c} - \frac{1}{\rho_i} \right).$$

Data from ice cores retrieved at Vostok and Komsomolskaya stations, and at 8 other drilling sites located at 60, 73, 105, 140, 200, 325, and 400 kilometers from the coast along the route Mirny-Vostok, and the published data from Byrd [43, 44] and Dye 3 [58] have been used to verify the link

between the number (size) of normal bubbles in the recent ice and the grain size at the pore close-off depth. For the wide range of temperatures ($-57\dots-20$ °C) and accumulation rates ($2\dots50$ gcm⁻²yr⁻¹) clear linear relationships between N_b and $1/A_c^{1.5}$, and between N_b and $1/\langle r_{bc} \rangle^3$ are confirmed. The values $\lambda \approx 3\pi$ and $y \approx 1.7$ are deduced from the data assuming a truncated-octahedron shape for the ice grains [31, 32].

Most of the observations of grain growth in polar firn support the linear relationship between the mean grain size A and the age of ice τ (e.g., Stephenson [59]; Gow [60, 61]), that is

$$A = A_0 + K\tau, \quad (10)$$

where A_0 is the average grain size at $\tau = 0$. The effective growth rate K primarily depends on temperature and in most experimental studies is assumed to have the Arrhenius form:

$$K = K' \exp(-Q/RT). \quad (11)$$

The age of ice at the firn-ice transition (τ_c) is, in turn, determined by the firn temperature and the rate of snow accumulation through the firn-densification process. A number of models have been proposed to represent the present-day density-depth profiles (e.g., Herron and Langway [62]; Barnola and others [63]; Arnaud and others [64]). Using either of them, τ_c can be obtained as

$$\tau_c = f(T, b, \rho_0, \rho_c), \quad (12)$$

where ρ_0 is the surface-snow density, T and b are the firn temperature and the accumulation rate prevailing over the time

of the snow-ice transformation, respectively. The present-day linear relationship $\rho_c(T)$, based on air-content measurements at 22 drilling sites [29] has been proposed [65] to describe relatively small change in the close-off density. This approach is commonly being used for dating the gas extracted from ice cores (e.g., Arnaud and others; Blunier and Schwander, this volume).

Because the grain-size-controlled bubble concentrations are both time and temperature dependent, the spatial and temporal changes in the air-bubble structure result mainly from changes in the temperature-accumulation relation. Using the system (9)–(12) with $Q = 46$ kJmole⁻¹, $K' = 4.2 \cdot 10^7$ mm²yr⁻¹, and $A_0 = 0.7$ mm² (the last two values correspond to the truncated-octahedron approximation [31]), and using a slightly modified Herron-Langway model for firn densification at stationary conditions and $\rho_0 = 0.36$ gcm⁻³, we calculated the number of normal bubbles in 1 g of polar ice as a function of temperature and accumulation rate [32]. The results are shown in Fig. 10 together with the present-day conditions at the drilling sites for which the data on bubble number are available. The deviations of modeled bubble concentrations from the data (including newly published results from GRIP [15] and Dome F [19] cores) are within ± 50 g⁻¹ (2σ).

Fig. 10 shows a clustering of N_b values within 370 ± 100 g⁻¹, which is attributed to a certain nonlinear correlation between site temperature and accumulation rate (which also underlies the present-day linear $\ln \tau_c(T)$ -relationship [61]). Therefore the new data from the sites with moderate temperature and relatively low accumulation rate (e.g., Siple Dome) and the cold

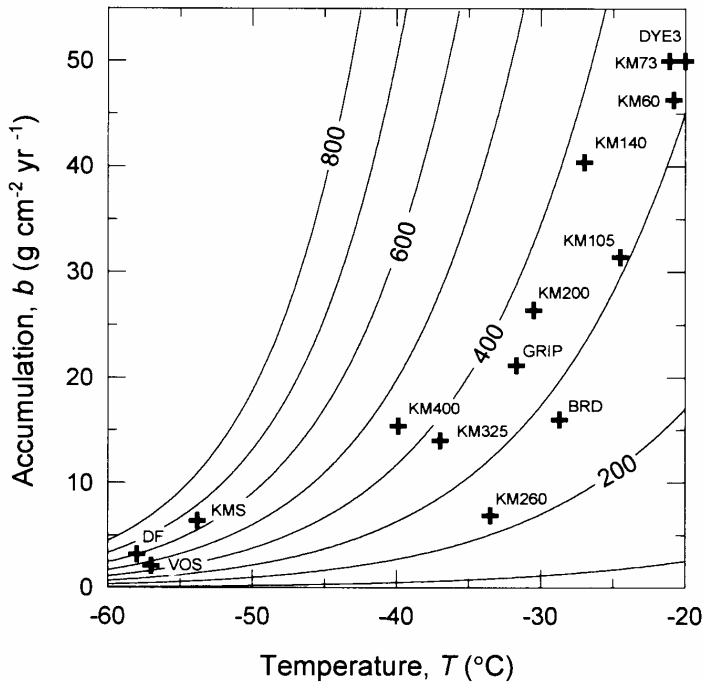


Figure 10: Number of air bubbles in 1 g of polar ice as a function of temperature and accumulation rate as calculated using the model described in the text. The crosses designate the present-day conditions at the polar sites for which the data on number concentration of air bubbles in recent ice are available.

sites with relatively high accumulation rate (e.g., South Pole) are particularly desirable to further constrain the model connecting the bubble (hydrate) geometrical properties with the ice formation conditions.

Application of the above model to the data on normal bubbles from the Vostok core [17, 18] has allowed to demonstrate that the increase of bubble concentration in LGM ice (see Fig. 2b) is due to a much stronger effect of grain-growth-rate slowdown (because of the low LGM temperature) than the effect of growth-time increase (because of the low temperature and accumulation rate) [31]. Moreover, the LGM-bubble concentration appears to be more consistent with the LGM temperature-accumulation relation inferred from borehole-temperature analysis (e.g.,

Salamatin, this volume) than that with the history obtained using the traditional approach to interpret isotope data (e.g., Petit and others [33]). Thus, it has been suggested [22] that the air-bubble and air-hydrate records in polar ice cores could be used to test the temperature-accumulation relations obtained from paleoclimatic reconstructions based on the ice-core data. This new, independent constraint on past climate change might become particularly useful when being incorporated into the isotope-borehole temperature calibration procedure based on heat- and ice-flow models (e.g., Cuffey and Clow [67]; Salamatin, this volume).

7. Conclusion

The bimodal pattern of bubble-size distributions and the observed difference in bubble pressures suggest existence of two generations of air bubbles in polar ice: the normal bubbles, which dominate number and volume concentrations, and are formed in the close-off zone (90–105 m at present time at Vostok); and the microbubbles, which represent only 0.3% of the air content and are trapped at shallower depths. Evolution of the bubble ensembles below the firm-ice transition involves post-closure disintegration of elongated normal bubbles, and compression of all bubbles in plastically-deforming ice matrix. The size and abundance of normal bubbles at the end of their disintegration (170 m) are controlled by the size of the ice grains during pore closure and thereby by the temperature and accumulation rate prevailing over the time of snow-ice transformation.

Below 170 m, the number-size distributions of both types of bubbles are separately log-normal and characterized by substantially constant relative variance of bubble radii equal to 0.40. Accordingly, the size distribution of the total-bubble population is bimodal and reaches a steady state with a relative variance of 0.48 below the 250-m depth where the pressure in all bubbles equalizes. The steady-state distributions of the different bubble populations hold until the start of the bubble-hydrate transition.

In the bubble-hydrate transition zone (500–1250 m) all bubbles progressively transform to hydrates. Clathrate nucleation clearly favors the smaller (or micro-) bubbles and therefore it is linked to bubble-size distribution. The net effect of diffusive gas transfer between coexisting bubbles and

hydrates on the geometrical properties of hydrates is small and by the end of transition (1000–1250 m) the relative variance of hydrate radii (0.49) is very nearly that of the total-bubble population (0.48) on the threshold of the transition.

Important modifications of the hydrate-size distribution occur in the depth range between 1100–1200 and 1500–1600 m, which is associated with transient period of hydrate-crystal coalescence (or crystal growth). By the end of this relatively short phase of hydrate evolution, most of the small crystals (originating mainly from microbubbles) dissolve in ice to the advantage of larger, growing hydrates. As a result, the hydrate number returns to a value nearly equal to the number of normal bubbles, although the hydrate-size distribution becomes narrower (relative variance is 0.30) than that of the all bubbles (0.48) and the normal bubbles (0.40) before the transition. In the subsequent, asymptotic phase of coalescence (1500–3310 m), crystal growth is very slow and the hydrate-size distribution remains fixed. Assuming that the size distributions of normal bubbles above the transition zone and air hydrates below 1500 m are in their steady states, and that air content of ice is constant, the size of the succeeding air hydrates can be determined from the size of preceding normal bubbles and vice versa. Thus, the climate signal imposed on the bubble properties at pore close-off can be completely recovered from the resulting number-size distributions of air hydrates.

These results suggest that the air-bubble and air-hydrate records in polar ice cores could be used to test the temperature-accumulation relations obtained from paleoclimatic reconstructions based on the ice-core data. Included into the isotope-

borehole temperature calibration procedure (based on heat- and ice-flow models), this new, independent constraint on past climate change might become particularly useful.

Acknowledgements

This work is part of a comprehensive study of air hydrates in polar ice cores that is an informal collaborative effort initiated in 1992 between LGGE (Grenoble), ILTS (Sapporo), Kazan State University (Kazan), and AARI (St. Petersburg). I am indebted to J.R. Petit, N.I. Barkov, P. Duval, and T. Hondoh for their long-standing support of this work at Vostok, AARI, LGGE and ILTS, and to A.N. Salamatin for his long-term collaboration and important contribution to this study. The work has gained much from useful discussions with T. Uchida, T. Ikeda, H. Narita, L. Arnaud, J-M. Barnola, D. Raynaud, S. Kipfstuhl, and W. Kuhs. This study was supported by grant N 99-05-65685 from the Russian Basic Research Foundation.

References

1. A.J. Gow, H.T. Ueda, and D.E. Garfield, *Science* **161** (1968) 1011.
2. S.L. Miller, *Science* **165** (1969) 489.
3. H. Shoji and C.C. Langway, Jr., *Nature* **298** (1982) 548.
4. T. Hondoh, H. Anzai, A. Goto, S. Mae, A. Higashi, and C.C. Langway, Jr., *J. Incl. Phenom. Molecul. Recogn. Chem.* **8** (1990) 17.
5. J-M. Barnola, D. Raynaud, Y.S. Korotkevich, and C. Lorius, *Nature* **329** (1987) 408.
6. A. Neftel, H. Oeschger, T. Staffelbach, and B. Stauffer, *Nature* **331** (1988) 609.
7. D. Raynaud, J. Jouzel, J-M. Barnola, J. Chappellaz, R. J. Delmas, and C. Lorius, *Science* **259** (1993) 926.
8. T. Sowers and 6 others, *Paleoceanography* **8** (1993) 737.
9. M. Bender, T. Sowers, and V.Ya. Lipenkov, *J. Geophys. Res.* **100** (1995) 18651.
10. M. Anklin and 6 others, *J. Geophys. Res.* **102** (1997) 26539.
11. A. Neftel, H. Oeschger, J. Schwander, and B. Stauffer, *J. Phys. Chem.* **87** (1983) 4116.
12. T. Ikeda and 7 others, *Geophys. Res. Lett.* **26** (1999) 91.
13. T. Uchida, T. Hondoh, S. Mae, V.Ya. Lipenkov, and P. Duval, *J. Glaciol.* **40** (1994) 79.
14. T. Uchida, T. Hondoh, S. Mae, V.Ya. Lipenkov, P. Duval, and J. Kawabata, *Proc. NIPR Symp. Polar Meteorol. Glaciol.* **8** (1994) 140.
15. F. Pauer, S. Kipfstuhl, W.F. Kuhs, and H. Shoji, *J. Glaciol.* **45** (1999) 22.
16. T. Ikeda, A.N. Salamatin, V.Ya. Lipenkov, and T. Hondoh, this volume.
17. N.I. Barkov and V.Ya. Lipenkov, *Mater. Glyatsiol. Issled.* **51** (1984) 178.
18. V.Ya. Lipenkov, *Mater. Glyatsiol. Issled.* **65** (1989) 58.
19. H. Narita and 8 others, *Ann. Glaciol.* **29** (1999) in press.
20. A.N. Salamatin, this volume.
21. N.I. Barkov and V.Ya. Lipenkov, *Problemy Arktiki i Antarktiki* **69** (1995) 92.
22. V.Ya. Lipenkov, P. Duval, T. Hondoh, A.N. Salamatin, and N.I. Barkov, *EOS Transactions AGU* **79** (1998) F152.

23. T. Hondoh, *Nihon Kessho Seicho Gakkai Shi* [J. Japanese Assoc. Crystal Growth] **16** (1989) 149.
24. T. Hondoh, In: *Proc. of 2nd Int. Conf. on Natural Gas Hydrates* (1996) 131.
25. A.N. Salamatin, T. Hondoh, T. Uchida, and V.Ya. Lipenkov, *J. Cryst. Growth* **193** (1998) 197.
26. A.N. Salamatin, V.Ya. Lipenkov, T. Hondoh, and T. Ikeda, *Ann. Glaciol.* **29** (1999) in press.
27. V.Ya. Lipenkov, and A.N. Salamatin, *Antarktika* **28** (1989) 59.
28. V.Ya. Lipenkov, N.I. Barkov, P. Martinerie, and D. Raynaud, *Antarktika* **31** (1993) 85.
29. P. Martinerie, V.Ya. Lipenkov, D. Raynaud, J. Chappellaz, N.I. Barkov, and C. Lorius, *J. Geophys. Res.* **99** (1994) 10565.
30. V.Ya. Lipenkov, A.N. Salamatin, and P. Duval, *J. Glaciol.* **43** (1997) 397.
31. V.Ya. Lipenkov, O.A. Ryskin, and N.I. Barkov, *Mater. Glyatsiol. Issled.* **86** (1999) 75.
32. V.Ya. Lipenkov, A.N. Salamatin, N.I. Barkov, P. Duval, and T. Hondoh, to be submitted.
33. J.R. Petit and 18 others, *Nature* **399** (1999) 429.
34. A.N. Salamatin and V.Ya. Lipenkov, *Antarctic Record, NIPR* **37** (1993) 265.
35. E.E. Underwood, *Addison-Wesley Publishing Company* (1970) 274.
36. S.A. Saltykov, *Moscow Metallurgiya* (1976) 235.
37. A.N. Salamatin, V.Ya. Lipenkov, and P. Duval, *J. Glaciol.* **43** (1997) 387.
38. S. Takeya, H. Nagaya, T. Hondoh, T. Matsuyama, and V.Ya. Lipenkov, *J. Phys. Chem. B* (2000) in press.
39. W.F. Kuhs, A. Klapproth, and B. Chazallon, this volume.
40. V.Ya. Lipenkov, F. Candaudap, J. Ravoire, E. Dulag, D. Raynaud, *J. Glaciol.* **41** (1995) 423.
41. R.B. Alley and J.J. Fitzpatrick, *J. Glaciol.* **45** (1999) 147.
42. P.F. Scholander and D.C. Nutt, *J. Glaciol.* **3** (1960) 671.
43. A.J. Gow and T. Williamson, *J. Geophys. Res.* **80** (1975) 5101.
44. A.J. Gow, *CRREL Res. Rep.* **249** (1968) 16.
45. T. Uchida, T. Hondoh, S. Mae, P. Duval, and V.Ya. Lipenkov, In: “*Physics and Chemistry of Ice*” eds. by S. Maeno and T. Hondoh, Hokkaido Univ. Press, Sapporo (1992) 121.
46. T. Uchida, T. Hondoh, S. Mae, P. Duval, and V.Ya. Lipenkov, *Ann. Glaciol.* **20** (1994) 143.
47. V.Ya. Lipenkov, N.I. Barkov, P. Duval, and P. Pimienta, *J. Glaciol.* **35** (1989) 392.
48. V.Ya. Lipenkov and N.I. Barkov, *International workshop on Lake Vostok, St. Petersburg* (1998) 31.
49. T. Uchida, S. Mae, T. Hondoh, P. Duval, and V.Ya. Lipenkov, *Proc. NIPR Symp. Polar Meteorol. Glaciol.* **7** (1993) 1.
50. T. Uchida, S. Mae, T. Hondoh, P. Duval, and V.Ya. Lipenkov, *Proc. NIPR Symp. Polar Meteorol. Glaciol.* **7** (1993) 7.
51. I.M. Lifshitz and V.V. Slyozov, *Zh. Eksp. Teor. Fiz.* **35** (1958) 479.
52. J. Jouzel and 9 others, *Science* **286** (1999) 2138.
53. A.N. Salamatin, R.N. Vostretsov, J.R. Petit, V.Ya. Lipenkov, and N.I. Barkov, *Mater. Glyatsiol. Issled.* **85** (1998) 233.
54. H. Shoji and C.C. Langway, Jr., *J. Phys. (Paris)* **48** (1987) C1-551.
55. T. Ikeda, T. Uchida, and S. Mae, *Proc. NIPR Symp. Polar Meteorol. Glaciol.* **7** (1993) 14.

56. V.Ya. Lipenkov, A.N. Salamatin, and Yu.A. Grigoryeva, *Mater. Glyatsiol. Issled.* **65** (1989) 49.
57. J. Ocampo, B. Schmitt, and J. Klinger, *J. Phys. (Paris)* **48** (1987) C1-557.
58. H. Shoji and C.C. Langway, Jr., *AGU Monograph* **33** Washington DC (1985) 39.
59. P.J. Stephenson, *Physics of Snow and Ice*, Sapporo **1** (1967) 725.
60. A.J. Gow, *J. Glaciol.* **8** (1969) 241.
61. A.J. Gow, *IAHS, Publ.* **114** (Snow Mechanics) (1975) 25.
62. M.M. Herron and C.C. Langway, Jr., *J. Glaciol.* **25** (1980) 373.
63. J-M. Barnola, P. Pimienta, D. Raynaud, and Y.S. Korotkevich, *Tellus B* **43** (1991) 83.
64. L. Arnaud, J-M. Barnola, and P. Duval, this volume.
65. J. Schwander and 6 others, *J. Geophys. Res.* **98** (1993) 2831.
66. T. Blunier and J. Schwander, this volume.
67. K.M. Cuffey and G.D. Clow, *J. Geophys. Res.* **102** (1997) 26383.